

Invariance on Manifolds: Understanding Robust Visual Representations for Place Recognition

Jintao Cheng*, Weibin Li**, Zhijian He*, Jin Wu***, Chi Man VONG** and Wei Zhang*

*The Hong Kong University of Science and Technology, Hong Kong, China

**University of Macau, Macau, China

***University of Science and Technology Beijing, Beijing, China

Abstract—Visual Place Recognition (VPR) demands representations robust to drastic environmental and viewpoint shifts. Current aggregation paradigms, however, either rely on data-hungry supervision or simplistic first-order statistics, often neglecting intrinsic structural correlations. In this work, we propose a Second-Order Geometric Statistics framework that inherently captures geometric stability without training. We conceptualize scenes as covariance descriptors on the Symmetric Positive Definite (SPD) manifold, where perturbations manifest as tractable congruence transformations. By leveraging geometry-aware Riemannian mappings, we project these descriptors into a linearized Euclidean embedding, effectively decoupling signal structure from noise. Our approach introduces a training-free framework built upon fixed, pre-trained backbones, achieving strong zero-shot generalization without parameter updates. Extensive experiments confirm that our method achieves highly competitive performance against state-of-the-art baselines, particularly excelling in challenging zero-shot scenarios.

Index Terms—Visual Position Recognition, Training-free, SPD manifold

I. INTRODUCTION

Visual Place Recognition (VPR) constitutes a cornerstone of long-term autonomous navigation, enabling robots to accurately localize within previously visited environments despite drastic changes in visual appearance [1], [2]. The fundamental challenge of this task stems from the stringent requirement to simultaneously satisfy two distinct and often conflicting objectives: **condition invariance** [3], [4] and **viewpoint invariance** [5], [6], as illustrated in Fig. 1. On one hand, environmental dynamics—such as day-to-night transitions, seasonal cycles, and weather fluctuations—induce drastic non-linear photometric distortions that severely degrade feature stability [7]. On the other hand, variations in the camera’s 6-DoF pose result in complex projective transformations, scale changes, and occlusions, thereby disrupting spatial correspondence [8]. Consequently, constructing a robust representation capable of withstanding these compounded perturbations while capturing the intrinsic essence of a scene remains a core scientific problem in the field.

To obtain such invariant representations, modern VPR methodologies have converged to a two-stage paradigm: a

J. Cheng, Z. He, and W. Zhang are with The Hong Kong University of Science and Technology (e-mail: Jchengau@connect.ust.hk; eeweiz@ust.hk). Corresponding author: Wei Zhang.

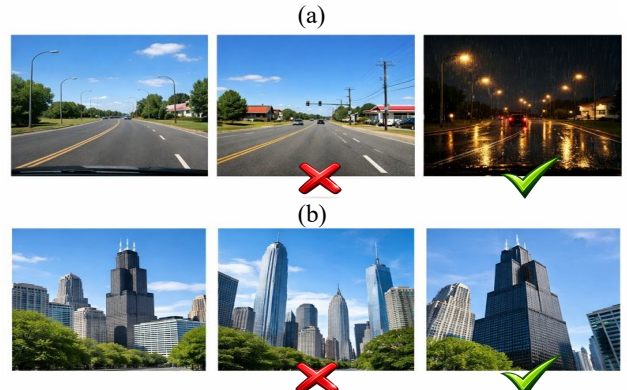


Fig. 1: Illustration of the two fundamental challenges in Visual Place Recognition (VPR). (a) Condition Invariance: The system must identify the correct match (right) despite drastic illumination and weather changes (e.g., sunny day vs. rainy night), while rejecting perceptually similar scenes from different locations (middle). (b) Viewpoint Invariance: The system must recognize the same landmark (right) under significant changes in scale and camera pose, distinguishing it from other similar-looking structures (middle).

feature extraction Backbone Φ and a global Aggregation Head Ψ . Specifically, the backbone Φ is responsible for extracting discriminative local features from raw images, while the aggregation head Ψ fuses these local cues into a compact global descriptor. Historically, extensive research efforts have been dedicated to training specialized backbones [6], [9], [10]. However, with the emergence of powerful visual foundation models represented by the DINO series [11], the capability to extract robust local features has become increasingly mature and generalized. Consequently, the bottleneck for achieving all-scenario invariance has decisively shifted to the aggregation module Ψ . The critical question now lies in how to organize these high-quality features to construct a global descriptor that remains stable under the aforementioned geometric and photometric transformations.

Existing aggregation methods primarily fall into two categories, yet both face distinct dilemmas. The first category is Supervised Implicit Aggregation [12], [13]. These methods

employ massive Multi-Layer Perceptrons (MLPs) or attention mechanisms, attempting to implicitly approximate the compositional rules between features through intensive training on specific datasets. However, this strategy essentially encodes domain-specific data-driven priors rather than learning general physical laws, leading to heavy reliance on training data and limited generalization capabilities in cross-domain scenarios. The second category is Unsupervised First-order Aggregation [14], [15]. To maintain an unsupervised nature, these methods often revert to rudimentary aggregation schemes, such as Generalized Mean (GeM) pooling [16] or VLAD clustering. While these methods based on First-order Statistics are general, they neglect the rich structural correlations among features, resulting in inherent sensitivity to environmental perturbations.

We advocate revisiting this problem from a geometric perspective to overcome these limitations. Drastic environmental changes (such as illumination scaling and viewpoint rotation) can be approximately modeled as affine transformations within the feature space. We demonstrate through theoretical derivation and extensive experiments that, first-order statistics (mean) are unstable and drift with transformations. However, second-order statistics (covariance) exhibit a unique advantage—they possess an intrinsic Congruence Property. This implies that the covariance matrix can naturally resist additive noise and maintain the consistency of the topological structure of feature distribution under multiplicative transformations. Mathematically, this second-order structure resides on the Symmetric Positive Definite (SPD) manifold [17]. This provides us with a theoretical foundation to achieve robustness relying solely on the intrinsic geometric properties of the data, without depending on parameter learning.

In this work, we introduce Riemannian Invariant Aggregation (RIA) operator, an explicit geometric modeling paradigm. RIA explicitly extracts the intrinsic second-order covariance structure of the scene, obviating the need for learned parameters to approximate structural information. We leverage Riemannian Manifold Mapping to project the non-Euclidean geometric structure into a statistically well-behaved tangent space, thereby achieving compatibility with standard Euclidean retrieval. By relying on analytical statistical properties rather than data-driven parameter fitting, RIA establishes a new training-free paradigm, which not only guarantees theoretical interpretability but also demonstrates superior Zero-shot Generalization capabilities in diverse and unseen domains.

The principal contributions of this work are summarized as follows:

1) We provide theoretical justifications from a Riemannian perspective, demonstrating that second-order statistics residing on the SPD manifold exhibit superior intrinsic invariance to viewpoint and illumination variations compared to conventional first-order aggregates.

2) We introduce the Riemannian Invariant Aggregation (RIA) operator. This training-free and computationally efficient module integrates second-order statistical representations with geometry-aware Riemannian mappings and statistical denoising mechanisms.

3) Extensive evaluations across diverse VPR benchmarks, encompassing a wide range of environmental conditions, demonstrate that our zero-shot approach achieves highly competitive performance against state-of-the-art baselines, particularly in challenging cross-domain scenarios. The source code will be released as open source.

II. RELATED WORK

A. Visual Place Recognition

Contemporary VPR pipelines generally adhere to a two-stage paradigm: extracting local features via a backbone and fusing them into a global descriptor. Early approaches primarily fine-tuned CNNs [9], [16], later evolving into massive classification frameworks to learn viewpoint robustness [6], [18]. With the advent of Vision Transformers, recent methods integrate attention mechanisms to capture long-range dependencies [10], [19]. While foundation models have demonstrated strong zero-shot capabilities [14], adapter-based approaches often re-introduce training phases to align features with the target domain [13], [20].

The aggregation module plays a pivotal role in encoding invariance. Traditional methods rely on first-order statistics or clustering mechanisms [9], [16], [21]. To capture complex structural relationships, supervised methods employ parameter-heavy MLPs or cross-image attention [12], [13], though they often suffer from limited generalization across domains. Conversely, unsupervised methods typically revert to rudimentary pooling or optimal transport schemes [14], [22] to maintain their training-free nature. Distinct from these approaches, our work explicitly models intrinsic second-order structures without relying on parameter learning or labeled supervision.

B. Deep Learning on SPD Manifolds

The integration of Riemannian geometry into deep neural networks has significantly advanced the processing of second-order statistics. This paradigm was pioneered by SPDNet [17], which generalized conventional CNN operations—such as bilinear mapping and eigenvalue rectification—to the SPD manifold. Building on this, DreamNet [23] bridged Euclidean and Riemannian domains to learn more discriminative deep representations. Subsequent research has focused on enhancing both representational power and training efficiency. Notable contributions include introducing Riemannian local mechanisms to capture fine-grained structure [24], meta-learning optimizers to handle manifold constraints [25], and exploring space quantization for efficient representation [26]. Besides, these architectural advancements have driven progress in metric and similarity learning, particularly for Image Set Classification. Huang et al. [27] proposed geometry-aware similarity learning to handle visual distortions, while Wang et al. [28] developed deep metric learning frameworks specifically tailored for set-based classification on the manifold.

However, the potential of SPD manifold learning in Visual Place Recognition (VPR) remains largely untapped. Unlike Image Set Classification, which typically operates in closed-set scenarios, VPR demands descriptors that are explicitly robust

to drastic, open-world environmental shifts and viewpoint deviations. Our work addresses this gap by leveraging the intrinsic geometry of SPD matrices to construct a second-order representation that ensures geometric stability in challenging open-world scenarios.

III. PRELIMINARIES

In this section, we formulate the geometric foundation of modeling image representations on the Symmetric Positive Definite (SPD) manifold. Throughout the paper, vectors are denoted by bold lower-case letters (e.g., \mathbf{x}), and matrices by bold upper-case letters (e.g., \mathbf{C}).

The SPD Manifold. The space of $d \times d$ Symmetric Positive Definite matrices, denoted as \mathcal{S}_{++}^d , is defined as:

$$\mathcal{S}_{++}^d = \left\{ \mathbf{M} \in \mathbb{R}^{d \times d} \mid \mathbf{M} = \mathbf{M}^\top, \mathbf{v}^\top \mathbf{M} \mathbf{v} > 0, \forall \mathbf{v} \in \mathbb{R}^d \setminus \{\mathbf{0}\} \right\}. \quad (1)$$

Geometrically, \mathcal{S}_{++}^d forms a convex cone endowed with a Riemannian metric. Standard Euclidean operations on this manifold ignore the intrinsic geodesic curvature, often leading to the “swelling effect,” where the determinant of the matrix increases artificially, introducing noise into the representation.

Power Euclidean Metric (PEM). To perform efficient retrieval while respecting the manifold geometry, we adopt the Power Euclidean Metric [29] framework. This maps the Riemannian manifold to a linearized metric space via a matrix power transformation. Given any two descriptors $\mathbf{C}_1, \mathbf{C}_2 \in \mathcal{S}_{++}^d$, the PEM distance with power $\alpha \in (0, 1]$ is defined as:

$$d_{\text{PEM}}(\mathbf{C}_1, \mathbf{C}_2) = \frac{1}{\alpha} \|\mathbf{C}_1^\alpha - \mathbf{C}_2^\alpha\|_F. \quad (2)$$

In this work, we focus on the matrix square root ($\alpha = 0.5$), which effectively flattens the manifold curvature and approximates the Riemannian geodesic distance. To validate the effectiveness of the power parameter α and determine its optimal value for our task, we conduct extensive experiments on this parameter, with detailed analyses and results presented in the section V-G.

Isometric Vectorization. To interface with standard vector-based search engines, a symmetric matrix \mathbf{M} must be flattened. To ensure this mapping $\psi: \mathcal{S}_{++}^d \rightarrow \mathbb{R}^{d(d+1)/2}$ is an isometry, the off-diagonal elements must be scaled:

$$\text{vec}(\mathbf{M}) = [m_{1,1}, \dots, m_{d,d}, \sqrt{2}m_{1,2}, \dots, \sqrt{2}m_{d-1,d}]^\top. \quad (3)$$

IV. METHODOLOGY

We propose the second-order geometric statistics framework, a training-free pipeline designed to extract robust geometric representations for VPR shown in 2. Our method transforms local deep features into a global descriptor on the SPD manifold through four logically coupled phases: (1) **feature projection and aggregation** to construct the compact covariance representation, (2) **sparse structural rectification** to suppress spurious correlations, (3) **iterative Riemannian linearization** to approximate the geodesic metric efficiently, and (4) **isometric**

vectorization to bridge the manifold geometry with Euclidean retrieval engines.

A. Feature Projection and Aggregation

Current VPR approaches typically rely on first-order pooled features, which suffer from perceptual aliasing, are sensitive to viewpoint changes, and lack robustness under illumination variations. We theoretically establish that second-order statistics effectively mitigate these issues by encoding structural correlations and offering inherent robustness to geometric and photometric transformations (see Appendix B, C); hence, we adopt the covariance matrix as a feature representation at this stage to enhance descriptor robustness.

Given an input image I , we utilize a pre-trained Visual Foundation Model to extract dense local representations. We extract a set of N patch-level local features, denoted as a matrix $\mathbf{X}_{\text{raw}} \in \mathbb{R}^{N \times D_{\text{in}}}$, where D_{in} represents the native feature dimension. To ensure the resulting covariance matrix is full-rank and strictly resides on the SPD manifold, we project the features into a lower-dimensional subspace \mathbb{R}^d ($d < N$) using a fixed random orthogonal matrix $\mathbf{P} \in \mathbb{R}^{D_{\text{in}} \times d}$:

$$\mathbf{X} = \mathbf{X}_{\text{raw}} \mathbf{P}, \quad (4)$$

where $\mathbf{X} = [\mathbf{x}_1, \dots, \mathbf{x}_N]^\top \in \mathbb{R}^{N \times d}$ represents the projected feature matrix. Here, $\mathbf{x}_i \in \mathbb{R}^d$ denotes the i -th projected local descriptor, which is the i -th row of \mathbf{X} treated as a column vector. Subsequently, we aggregate these descriptors into a global sample covariance matrix $\mathbf{C}_{\text{raw}} \in \mathbb{R}^{d \times d}$:

$$\mathbf{C}_{\text{raw}} = \frac{1}{N-1} \sum_{i=1}^N (\mathbf{x}_i - \bar{\mathbf{x}})(\mathbf{x}_i - \bar{\mathbf{x}})^\top, \quad (5)$$

where $\bar{\mathbf{x}} = \frac{1}{N} \sum_{i=1}^N \mathbf{x}_i$ is the mean feature vector.

B. Sparse Structural Rectification

Sample covariance matrices derived from high-dimensional deep features often serve as noisy estimators of the underlying scene geometry. Specifically, when the feature dimension d is large relative to the number of patches N , the off-diagonal entries of \mathbf{C}_{raw} are prone to spurious correlations that distort the Riemannian structure. To recover the latent salient structure, we employ a Rectified Covariance(ReCov) mechanism, which can be viewed as a non-linear thresholding operator $\mathcal{R}_\tau(\cdot)$ aimed at consistent covariance estimation in high dimensions.

We define the rectified matrix $\mathbf{C}_{\text{rec}} = \mathcal{R}_\tau(\mathbf{C}_{\text{raw}})$ element-wise as:

$$[\mathbf{C}_{\text{rec}}]_{ij} = \begin{cases} [\mathbf{C}_{\text{raw}}]_{ij} & \text{if } i = j \text{ or } |[\mathbf{C}_{\text{raw}}]_{ij}| > \tau, \\ 0 & \text{otherwise,} \end{cases} \quad (6)$$

where $\tau \geq 0$ is the structural saliency threshold. Hard thresholding enables consistent estimation of sparse covariance matrices by removing noise-induced correlations while preserving dominant structural components. Although it may compromise positive definiteness, the subsequent regularization step ensures geometric integrity on the SPD manifold.

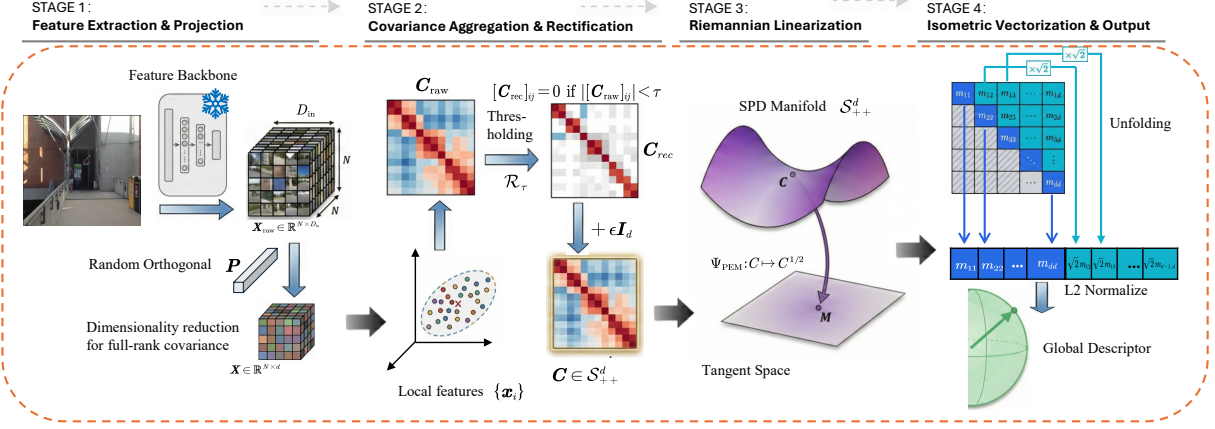


Fig. 2: **Schematic overview of the proposed Riemannian Invariant Aggregation (RIA) framework.** The pipeline transforms local features from a frozen backbone into a robust global descriptor through four geometric phases: **Stage 1:** High-dimensional features are projected onto a lower-dimensional subspace to ensure a full-rank covariance estimation. **Stage 2:** We compute the sample covariance and apply ReCov to suppress spurious noise. **Stage 3:** The covariance descriptor on the SPD manifold is mapped to a linearized tangent space via the PEM, approximated by Newton-Schulz iterations. **Stage 4:** The matrix is flattened using isometric vectorization (scaling off-diagonals by $\sqrt{2}$) and L_2 normalized to produce the final retrieval-ready descriptor. The entire process is training-free and parameter-efficient.

To ensure the resulting matrix strictly resides in the interior of the SPD manifold and to maintain numerical stability during the subsequent matrix square root computation, we apply the following regularization to obtain the final SPD descriptor \mathbf{C} :

$$\mathbf{C} = \mathbf{C}_{\text{rec}} + \epsilon \mathbf{I}_d, \quad (7)$$

where $\mathbf{C} \in \mathcal{S}_{++}^d$ represents the regularized covariance matrix, $\mathbf{I}_d \in \mathbb{R}^{d \times d}$ denotes the identity matrix, and $\epsilon > 0$ is a small regularization constant. This step effectively shifts the eigenvalues away from zero, yielding a strictly positive definite representation that captures the stable second-order geometric signature of the scene.

C. Iterative Riemannian Linearization

A core challenge in manifold learning involves comparing descriptors using the intrinsic geodesic distance, which is computationally expensive due to its heavy reliance on matrix logarithms and inversions. To circumvent this, we adopt the PEM framework to map the curved Riemannian manifold to a linearized metric space where Euclidean operations remain geometry-aware. Formally, our objective is to compute the matrix square root $\mathbf{C}^{1/2}$ for the regularized covariance matrix $\mathbf{C} \in \mathcal{S}_{++}^d$.

While $\mathbf{C}^{1/2}$ can be obtained via standard Eigenvalue Decomposition (EIG), this approach typically exhibits $O(d^3)$ complexity and gradient instability on GPU devices. Instead, we employ the coupled Newton-Schulz iteration [30] for an efficient numerical approximation. Since this iterative process converges locally only when the spectral radius is less than one, we first perform pre-normalization:

$$\mathbf{A}_0 = \frac{1}{\|\mathbf{C}\|_F} \mathbf{C}, \quad (8)$$

where $\|\mathbf{C}\|_F = \sqrt{\text{tr}(\mathbf{C}^\top \mathbf{C})}$ denotes the Frobenius norm. This normalization ensures the eigenvalues of \mathbf{A}_0 reside within the convergence domain $(0, 1]$. We then apply the coupled update rules for $k = 1, \dots, K$. Initializing $\mathbf{Y}_0 = \mathbf{A}_0$ and $\mathbf{Z}_0 = \mathbf{I}_d$, the iteration proceeds as:

$$\mathbf{Y}_k = \frac{1}{2} \mathbf{Y}_{k-1} (3\mathbf{I}_d - \mathbf{Z}_{k-1} \mathbf{Y}_{k-1}), \quad (9)$$

$$\mathbf{Z}_k = \frac{1}{2} (3\mathbf{I}_d - \mathbf{Z}_{k-1} \mathbf{Y}_{k-1}) \mathbf{Z}_{k-1}, \quad (10)$$

where \mathbf{Y}_k and \mathbf{Z}_k are the iterative approximations of the square root and the inverse square root of \mathbf{A}_0 , respectively.

After K iterations, the matrix \mathbf{Y}_K provides a numerical approximation of $\mathbf{A}_0^{1/2}$. To recover the original physical scale of the representation, we perform a post-compensation step to obtain the final mapped descriptor \mathbf{M} :

$$\mathbf{M} = \mathbf{Y}_K \sqrt{\|\mathbf{C}\|_F}. \quad (11)$$

This compensation is essential because the pre-normalization in Eq. (8) rescales the spectral energy of the matrix; failing to counteract this scaling would destroy the magnitude information of the original covariance, which carries critical discriminative cues for place recognition.

D. Isometric Vectorization

The final phase of our framework involves projecting the linearized manifold representation into a Euclidean space suitable for high-speed indexing. To faithfully preserve the geometric properties of the SPD manifold during this transformation, we adopt the mapping $\psi : \text{Sym}(d) \rightarrow \mathbb{R}^D$ ($D = d(d+1)/2$) defined in Equation 3. This mapping converts a symmetric matrix \mathbf{M} into a global descriptor \mathbf{v} .

The inclusion of the $\sqrt{2}$ scaling factor for off-diagonal entries is not a mere heuristic but a mathematical prerequisite to establish a Hilbert space isomorphism. As proven in Appendix E, this weighting ensures that the Euclidean inner product between any two vectorized descriptors \mathbf{v}_a and \mathbf{v}_b is strictly equivalent to the Frobenius inner product of their corresponding manifold points:

$$\langle \mathbf{v}_a, \mathbf{v}_b \rangle = \langle \mathbf{M}_a, \mathbf{M}_b \rangle_F = \text{tr}(\mathbf{M}_a \mathbf{M}_b). \quad (12)$$

By establishing this isomorphism, we guarantee that the L_2 normalization of \mathbf{v} correctly maps the descriptor onto a unit hypersphere while maintaining the structural correlations captured by the SPD manifold. Crucially, as detailed in Appendix C, this normalization, when coupled with the PEM mapping, grants the descriptor intrinsic invariance to global intensity fluctuations.

Geometric Integrity. The significance of this isometric embedding is that it allows standard Euclidean retrieval algorithms to operate as if they were performing computations directly on the manifold tangent space. By ensuring that $\mathbf{v}_a^\top \mathbf{v}_b$ faithfully represents the second-order structural similarity, our framework maintains high discriminative power and geometric stability during large-scale place recognition, effectively bridging Riemannian theory with practical search efficiency.

V. EXPERIMENTS

A. Compared Baselines

To comprehensively evaluate the effectiveness of our proposed framework, we benchmark it against two distinct categories of state-of-the-art VPR methods: supervised approaches requiring extensive labeled data, and unsupervised methods leveraging pre-trained foundation models.

Supervised Learning Baselines. These methods rely on large-scale datasets with GPS or pose labels to learn discriminative representations. We compare against three representative architectures. NetVLAD [9] serves as a seminal end-to-end trainable architecture that aggregates local descriptors based on residuals relative to learnable cluster centers, remaining a standard benchmark for aggregation capability. In a classification-based paradigm, CosPlace [6] reformulates VPR as a massive classification task, training a backbone on millions of images to recognize specific places while utilizing Generalized Mean (GeM) pooling for scale robustness. We also include MixVPR [12], a highly competitive MLP-based method which introduces a holistic architecture employing Feature-Mixer blocks to implicitly model global relationships and scene layout across feature maps.

Unsupervised Learning Baselines. In the unsupervised regime, methods leverage frozen visual backbones without task-specific fine-tuning. We primarily benchmark against AnyLoc [14], a robust general-purpose baseline that processes features from self-supervised Transformers (DINO and DINOv2) via PCA reduction and VLAD aggregation. We report results for both *AnyLoc-VLAD-DINO* and *AnyLoc-VLAD-DINOv2*. Crucially, although VLAD achieves strong unsupervised performance through the use of domain-specific

vocabularies, it still incurs a high clustering cost and therefore cannot be considered truly plug-and-play. In contrast, our method is entirely training-free and does not rely on any form of clustering.

B. Implementation Details

We utilize the pre-trained DINOv2-Giant [31] (frozen) as the backbone. Following AnyLoc [14], dense local descriptors are extracted from the 31st Transformer layer. Input images are resized to multiples of the 14×14 patch size. Feature aggregation employs a random projection to a lower-dimensional subspace to ensure full-rank covariance estimation. Structural rectification utilizes $\tau = 0$ and $\epsilon = 10^{-4}$. Riemannian linearization is performed via $K = 3$ Newton-Schulz iterations. All experiments are conducted on an NVIDIA A100 GPU.

a) Datasets: To evaluate the robustness and generalization of our method, we conduct experiments on a diverse set of seven challenging Visual Place Recognition benchmarks: 17places [32], Tokyo24/7 [33], Baidu [34], Pitts30k [35], Gardens [36], [37], Oxford [38], and St. Lucia [39]. These datasets represent a wide range of conditions including urban, suburban, and natural environments, as well as varying viewpoints, illumination, and seasonal changes. Performance is reported using the standard Recall@K metric (with K=1 and K=5), measuring the percentage of queries where the correct match is found within the top-K retrieved results, providing a comprehensive evaluation against state-of-the-art methods.

C. Main Results

Table I presents a comprehensive quantitative evaluation across seven diverse benchmarks. The results empirically validate that our RIA operator establishes a new state-of-the-art for training-free VPR, while exhibiting remarkable competitiveness against fully supervised approaches.

RIA demonstrates exceptional zero-shot generalization capability. A critical observation is the performance inversion on the challenging Tokyo 247 dataset, which contains drastic illumination changes (day-to-night). While supervised methods like NetVLAD [9] (60.6%) and CosPlace [6] (81.9%) struggle due to domain shifts, our training-free DINOv2-RIA achieves **89.2% R@1**. Notably, it surpasses the current supervised baseline, MixVPR (85.1%), by a margin of 4.1%. This confirms our theoretical proposition: second-order statistics on the SPD manifold possess intrinsic illumination invariance (via congruence transformation) that data-driven MLPs fail to capture without specific training samples. Similarly, on Oxford, which features significant viewpoint variations, our method achieves **98.4% R@1**, significantly outperforming the supervised CosPlace (95.3%) and NetVLAD (57.6%). This demonstrates that geometric stability is more transferable than learned semantic priors.

RIA exhibits advantages beyond first-order aggregation. To isolate the geometric contribution, we compare RIA against standard baselines (GeM, VLAD) sharing the identical DINOv2 backbone. RIA consistently dominates: on Oxford, it yields a **+15.7%** gain over DINOv2-VLAD; on St. Lucia, it outperforms

TABLE I: **Comparison with state-of-the-art methods across multiple VPR benchmarks.** We report Recall@1 (R@1) and Recall@5 (R@5) in percentages. The proposed **DINOv2-RIA** establishes a new training-free baseline, achieving competitive results against supervised methods and outperforming existing unsupervised approaches in most scenarios.

Method	17places		Tokyo24/7		Baidu		Pitts30k		Gardens		Oxford		St. Lucia	
	R@1	R@5	R@1	R@5	R@1	R@5								
<i>Supervised Learning</i>														
NetVLAD [9]	61.6	77.8	60.6	68.9	53.1	70.5	86.1	92.7	58.5	85.0	57.6	79.1	57.9	73.0
CosPlace [6]	61.1	76.1	81.9	90.2	41.6	55.0	90.4	95.7	74.0	94.5	95.3	99.5	99.6	99.9
MixVPR [12]	63.8	78.8	85.1	91.7	64.4	80.3	91.5	95.5	91.5	96.0	92.7	99.5	99.7	100.0
<i>Unsupervised Learning (with pre-trained backbone)</i>														
DINOv2-VLAD	64.2	81.2	85.7	89.8	63.7	79.8	85.7	93.9	96.5	100.0	82.7	92.6	96.5	99.1
AnyLoc-VLAD-DINO-PCA [14]	63.8	78.8	-	-	61.2	78.3	83.4	92.0	95.0	98.5	82.2	99.0	88.5	94.9
AnyLoc-VLAD-DINOv2-PCA [14]	64.8	81.0	-	-	74.9	89.4	86.9	93.8	96.0	99.5	96.9	100.0	96.4	99.5
<i>training-free (with pre-trained backbone)</i>														
DINOv2-GeM	63.7	80.0	83.1	94.2	63.5	77.7	83.6	92.3	89.5	99.0	88.4	94.7	89.0	95.6
DINOv2-RIA (ours)	64.7	81.2	89.2	92.3	67.5	80.3	86.7	93.8	97.5	99.5	98.4	100.0	97.2	98.7

TABLE II: **Ablation Study on Backbone Architectures and Aggregation Methods.** We compare our proposed RIA operator against standard aggregation schemes (GeM and VLAD) across diverse backbone types, including CNN-based (ResNet50) and Transformer-based (DINOv2, DINOv3) models.

Backbone	Aggregator	17places		Tokyo24/7		Baidu Dataset		Pitts30k	
		R@1	R@5	R@1	R@5	R@1	R@5	R@1	R@5
ResNet50	GeM	61.3	77.8	41.9	60.3	44.9	66.6	58.3	78.4
	VLAD	61.3	78.5	56.1	67.6	58.1	75.1	50.0	69.1
	RIA (Ours)	63.3	78.8	61.9	73.3	67.2	80.7	66.3	77.7
DINOv2-1B	GeM	63.7	80.0	83.1	94.2	63.5	77.7	83.6	92.3
	VLAD	64.2	81.2	85.7	89.8	63.7	79.8	85.7	93.9
	RIA (Ours)	64.7	81.2	89.2	92.3	67.5	80.3	86.7	93.8
DINOv3-0.3B	GeM	63.7	78.5	62.2	79.0	53.7	72.2	80.8	91.0
	VLAD	63.0	79.8	58.0	76.1	53.3	69.9	79.4	90.8
	RIA (Ours)	64.5	81.7	90.4	96.8	68.4	78.2	86.8	93.0

DINOv2-GeM by **+8.2%**. These margins prove that first-order pooling discards critical structural correlations, whereas preserving the covariance structure retains the unique geometric “fingerprint” of the scene.

Supervised methods (MixVPR [12]) retain a lead on datasets like Pitts30k (91.5% vs. 86.7%). This is expected, as MixVPR is trained on the massive GSV-Cities dataset. Since GSV-Cities shares a highly similar urban distribution with Pitts30k, supervised models benefit from substantial domain alignment. Conversely, our framework delivers highly competitive accuracy in a strictly zero-shot manner, without relying on any prior distribution.

D. Backbone Ablation Analysis

To verify the generalizability of our Riemannian Invariant Aggregation (RIA) framework across different feature extraction architectures, we conduct a comprehensive ablation study using three distinct backbones: the CNN-based ResNet50 (pre-trained on ImageNet), the standard ViT-based DINOv2-1B, and the latest DINOv3-0.3B. The results, summarized in Table II, allow us to disentangle the contribution of the aggregation module from the inherent strength of the feature extractor.

Crucially, RIA provides larger relative gains for weaker backbones. For instance, on the Baidu dataset, RIA improves the legacy ResNet50 performance by **+9.1%** over VLAD

(58.1% \rightarrow 67.2%), whereas the gain on the stronger DINOv2 is more moderate (+3.8%). This indicates that when local features lack semantic robustness, RIA’s explicit geometric modeling effectively compensates for backbone deficiencies, serving as a powerful structural prior that significantly boosts less discriminative models.

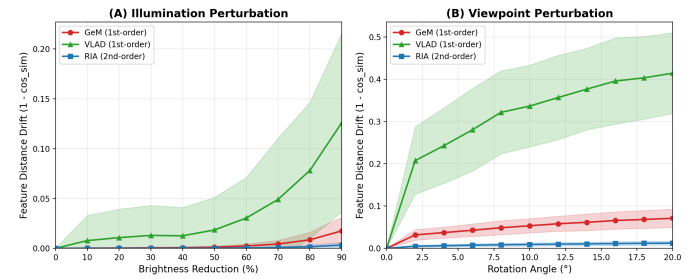


Fig. 3: Feature distance drift under illumination and viewpoint changes.

E. Empirical Verification of Structural Invariance

To validate geometric stability, we analyze feature drift ($1 - \cosine_similarity$) on 100 Pitts30k images under synthetic perturbations, as shown in Figure 3.

While first-order baselines (VLAD, GeM) degrade significantly under brightness reduction, RIA maintains a negligible drift (< 0.005). This empirically supports our proof in Appendix C, confirming that the homogeneity of the Power-Euclidean Metric naturally neutralizes global intensity scalings ($s^2 C$) without requiring learnable normalization.

Under planar rotation, VLAD diverges catastrophically due to quantization errors. In contrast, RIA exhibits exceptional stability. As derived in Appendix B, our metric treats rotation as a congruence transformation (QCQ^\top), effectively decoupling the intrinsic scene geometry from extrinsic camera pose.

F. Impact of Statistical Order and Manifold Geometry

To investigate the individual contributions of statistical order and geometric constraints, we conduct a controlled ablation

TABLE III: **Analysis of Statistical Order and Manifold Geometry.** We compare representations with different statistical orders (1st vs. 2nd) and geometric mappings (Euclidean vs. Riemannian). **Power-Euclidean Covariance (Ours)** utilizes the matrix square root to achieve the optimal trade-off on the Riemannian manifold.

Representation Method	Statistical Order	Geometric Mapping	Operator	Pitts30k R@1	Tokyo24/7 R@1
Magnitude Pooling	1st Order	Euclidean	Mean (GeM)	83.6	83.1
Euclidean Covariance	2nd Order	Euclidean	Identity	82.2	73.6
Log-Euclidean Covariance	2nd Order	Riemannian	Matrix Log	86.1	88.2
Power-Euclidean Covariance	2nd Order	Riemannian	Matrix Sqrt	86.7	89.2

study on the Pitts30k and Tokyo24/7 datasets, as summarized in Table III.

Counter-intuitively, simply elevating representations to second-order (Euclidean Covariance) without geometric correction degrades performance compared to first-order pooling (83.6% \rightarrow 82.2% on Pitts30k). This deterioration provides empirical evidence for the “swelling effect” discussed in Sec. III, confirming that treating the convex cone of SPD matrices as a flat Euclidean space distorts intrinsic distances.

TABLE IV: **Impact of the Power Parameter α on Pitts30k.** The parameter α controls the degree of metric deformation, interpolating between the Euclidean geometry ($\alpha = 1.0$) and the Log-Euclidean geometry ($\alpha \rightarrow 0$). Our choice of $\alpha = 0.5$ (Matrix Square Root) achieves the best Recall@1 performance.

Power Parameter	R@1	R@5	R@10
$\alpha = 1.0$ (Euclidean)	82.2	92.6	94.8
$\alpha = 0.75$	83.5	93.2	95.3
$\alpha = 0.5$	86.7	93.8	97.5
$\alpha = 0.25$	85.6	93.7	95.8
$\alpha = 0.1$	86.0	93.8	96.0
$\alpha \rightarrow 0$ (Log-Euclidean)	86.1	94.0	96.1

Properly incorporating Riemannian geometry (LEM or PEM) reverses this trend, yielding substantial gains (+4.5%) over the naive baseline. This improvement validates our core hypothesis: robustness stems from the *structure* of the data manifold, not just the information content of the statistics. Notably, our Power-Euclidean Covariance achieves the optimal trade-off (86.7%); as proven in Appendix C, the matrix square root offers superior scale invariance and numerical stability compared to the matrix logarithm, particularly near manifold boundaries.

G. Effect of Metric Deformation via the Power Parameter

To elucidate the geometric mechanism behind our representation, we investigate the sensitivity of the framework to the power parameter $\alpha \in (0, 1]$. This parameter controls the degree of metric deformation applied to the Symmetric Positive Definite (SPD) manifold, effectively interpolating between the Euclidean geometry ($\alpha = 1$) and the Riemannian Log-Euclidean geometry ($\alpha \rightarrow 0$).

As shown in Table IV, treating SPD matrices as points in a flat Euclidean space ($\alpha = 1.0$) yields the lowest performance (82.2% R@1), highlighting the necessity of geometric rectification. Decreasing α progressively flattens the manifold curvature, leading to consistent performance gains.

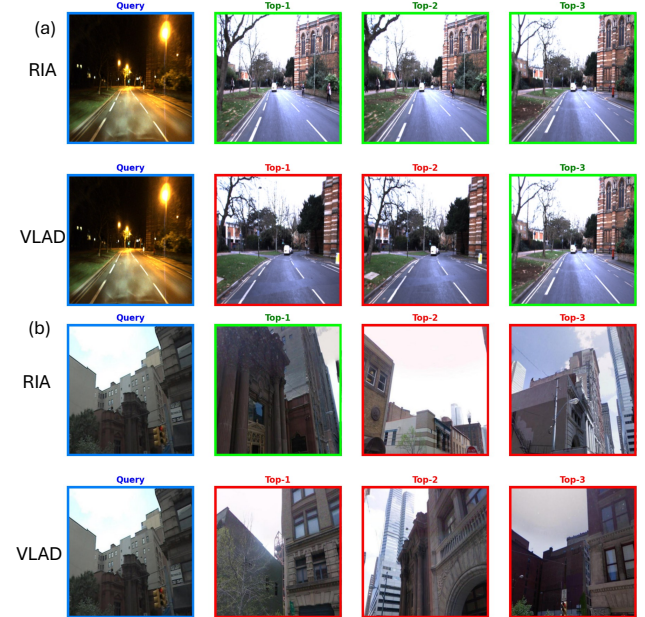


Fig. 4: **Qualitative comparison of Top-3 retrieval results.** Comparison between our RIA (top row) and the VLAD baseline (bottom row). (a) Under drastic illumination changes (Night-to-Day on Tokyo24/7), RIA successfully retrieves the correct scene. (b) Under viewpoint and scale variations (Pitts30k), RIA accurately identifies the landmark. Green and red borders indicate correct and incorrect matches, respectively.

Notably, our choice of $\alpha = 0.5$ (matrix square root) achieves the optimal R@1 of 86.7%, slightly outperforming the Log-Euclidean limit ($\alpha \rightarrow 0$, 86.1%). This suggests that the matrix square root provides a superior trade-off, offering sufficient geometric linearization to approximate geodesic distances while maintaining better numerical stability and noise robustness than the matrix logarithm for high-dimensional descriptors.

H. Example Visualization of Results

Figure 4 visualizes retrieval quality under two critical invariance tests. **(a) Condition Invariance:** In drastic night-to-day transitions, standard VLAD fails due to severe pixel-level domain shifts. In contrast, RIA successfully retrieves the structurally identical scene, validating its illumination robustness. **(b) Viewpoint Invariance:** We explicitly highlight a **highly difficult case** featuring extreme perspective distortion

and limited visual overlap. While VLAD is misled by superficial textures, RIA accurately identifies the landmark. This demonstrates that by modeling the scene's intrinsic geometry on the manifold, our method maintains discriminability even under severe spatial perturbations where first-order statistics collapse.

VI. CONCLUSION

We presented Riemannian Invariant Aggregation (RIA), a training-free VPR framework that models scenes as covariance descriptors on the SPD manifold. By exploiting the congruence invariance of second-order statistics and using Riemannian-aware mapping, RIA achieves strong zero-shot generalization with theoretical robustness to illumination and viewpoint changes. Experiments show that our zero-shot approach achieves highly competitive performance against state-of-the-art baselines.

REFERENCES

- [1] S. Lowry, N. Sünderhauf, P. Newman, J. J. Leonard, D. Cox, P. Corke, and M. J. Milford, “Visual place recognition: A survey,” *ieee transactions on robotics*, vol. 32, no. 1, pp. 1–19, 2015.
- [2] X. Zhang, L. Wang, and Y. Su, “Visual place recognition: A survey from deep learning perspective,” *Pattern Recognition*, vol. 113, p. 107760, 2021.
- [3] M. J. Milford and G. F. Wyeth, “Seqslam: Visual route-based navigation for sunny summer days and stormy winter nights,” in *2012 IEEE international conference on robotics and automation*, pp. 1643–1649, IEEE, 2012.
- [4] T. Sattler, W. Maddern, C. Toft, A. Torii, L. Hammarstrand, E. Stenborg, D. Safari, M. Okutomi, M. Pollefeys, J. Sivic, *et al.*, “Benchmarking 6dof outdoor visual localization in changing conditions,” in *Proceedings of the IEEE conference on computer vision and pattern recognition*, pp. 8601–8610, 2018.
- [5] S. Hausler, S. Garg, M. Xu, M. Milford, and T. Fischer, “Patch-netvlad: Multi-scale fusion of locally-global descriptors for place recognition,” in *Proceedings of the IEEE/CVF conference on computer vision and pattern recognition*, pp. 14141–14152, 2021.
- [6] G. Berton, C. Masone, and B. Caputo, “Rethinking visual geo-localization for large-scale applications,” in *Proceedings of the IEEE/CVF Conference on Computer Vision and Pattern Recognition*, pp. 4878–4888, 2022.
- [7] M. Zaffar, S. Garg, M. Milford, J. Kooij, D. Flynn, K. McDonald-Maier, and S. Ehsan, “Vpr-bench: An open-source visual place recognition evaluation framework with quantifiable viewpoint and appearance change,” *International Journal of Computer Vision*, vol. 129, no. 7, pp. 2136–2174, 2021.
- [8] F. Warburg, S. Hauberg, M. Lopez-Antequera, P. Gargallo, Y. Kuang, and J. Civera, “Mapillary street-level sequences: A dataset for lifelong place recognition,” in *Proceedings of the IEEE/CVF conference on computer vision and pattern recognition*, pp. 2626–2635, 2020.
- [9] R. Arandjelovic, P. Gronat, A. Torii, T. Pajdla, and J. Sivic, “Netvlad: Cnn architecture for weakly supervised place recognition,” in *Proceedings of the IEEE conference on computer vision and pattern recognition*, pp. 5297–5307, 2016.
- [10] S. Zhu, L. Yang, C. Chen, M. Shah, X. Shen, and H. Wang, “R2former: Unified retrieval and reranking transformer for place recognition,” in *Proceedings of the IEEE/CVF Conference on Computer Vision and Pattern Recognition*, pp. 19370–19380, 2023.
- [11] H. Zhang, F. Li, S. Liu, L. Zhang, H. Su, J. Zhu, L. M. Ni, and H.-Y. Shum, “Dino: Detr with improved denoising anchor boxes for end-to-end object detection,” *arXiv preprint arXiv:2203.03605*, 2022.
- [12] A. Ali-Bey, B. Chaib-Draa, and P. Giguere, “Mixvpr: Feature mixing for visual place recognition,” in *Proceedings of the IEEE/CVF winter conference on applications of computer vision*, pp. 2998–3007, 2023.
- [13] F. Lu, X. Lan, L. Zhang, D. Jiang, Y. Wang, and C. Yuan, “Cricavpr: Cross-image correlation-aware representation learning for visual place recognition,” in *Proceedings of the IEEE/CVF Conference on Computer Vision and Pattern Recognition*, pp. 16772–16782, 2024.
- [14] N. Keetha, A. Mishra, J. Karhade, K. M. Jatavallabhula, S. Scherer, M. Krishna, and S. Garg, “Anyloc: Towards universal visual place recognition,” *IEEE Robotics and Automation Letters*, vol. 9, no. 2, pp. 1286–1293, 2023.
- [15] C. Malone, S. Hussaini, T. Fischer, and M. Milford, “A hyperdimensional one place signature to represent them all: Stackable descriptors for visual place recognition,” in *Proceedings of the IEEE/CVF International Conference on Computer Vision*, pp. 9822–9833, 2025.
- [16] F. Radenović, G. Tolias, and O. Chum, “Fine-tuning cnn image retrieval with no human annotation,” *IEEE transactions on pattern analysis and machine intelligence*, vol. 41, no. 7, pp. 1655–1668, 2018.
- [17] Z. Huang and L. Van Gool, “A riemannian network for spd matrix learning,” in *Proceedings of the AAAI conference on artificial intelligence*, vol. 31, 2017.
- [18] G. Berton, G. Trivigno, B. Caputo, and C. Masone, “Eigenplaces: Training viewpoint robust models for visual place recognition,” in *Proceedings of the IEEE/CVF International Conference on Computer Vision*, pp. 11080–11090, 2023.
- [19] R. Wang, Y. Shen, W. Zuo, S. Zhou, and N. Zheng, “Transvpr: Transformer-based place recognition with multi-level attention aggregation,” in *Proceedings of the IEEE/CVF Conference on Computer Vision and Pattern Recognition*, pp. 13648–13657, 2022.
- [20] F. Lu, L. Zhang, X. Lan, S. Dong, Y. Wang, and C. Yuan, “Towards seamless adaptation of pre-trained models for visual place recognition,” *arXiv preprint arXiv:2402.14505*, 2024.
- [21] F. Lu, X. Zhang, C. Ye, S. Dong, L. Zhang, X. Lan, and C. Yuan, “Supervlad: Compact and robust image descriptors for visual place recognition,” *Advances in Neural Information Processing Systems*, vol. 37, pp. 5789–5816, 2024.
- [22] S. Izquierdo and J. Civera, “Optimal transport aggregation for visual place recognition,” in *Proceedings of the ieee/cvf conference on computer vision and pattern recognition*, pp. 17658–17668, 2024.
- [23] R. Wang, X.-J. Wu, Z. Chen, T. Xu, and J. Kittler, “Dreamnet: A deep riemannian manifold network for spd matrix learning,” in *Proceedings of the Asian conference on computer vision*, pp. 3241–3257, 2022.
- [24] Z. Chen, T. Xu, X.-J. Wu, R. Wang, Z. Huang, and J. Kittler, “Riemannian local mechanism for spd neural networks,” in *Proceedings of the AAAI Conference on Artificial Intelligence*, vol. 37, pp. 7104–7112, 2023.
- [25] Z. Gao, Y. Wu, Y. Jia, and M. Harandi, “Learning to optimize on spd manifolds,” in *Proceedings of the IEEE/CVF Conference on Computer Vision and Pattern Recognition*, pp. 7700–7709, 2020.
- [26] F. Tang, M. Fan, and P. Tiño, “Generalized learning riemannian space quantization: A case study on riemannian manifold of spd matrices,” *IEEE Transactions on Neural Networks and Learning Systems*, vol. 32, no. 1, pp. 281–292, 2020.
- [27] Z. Huang, R. Wang, X. Li, W. Liu, S. Shan, L. Van Gool, and X. Chen, “Geometry-aware similarity learning on spd manifolds for visual recognition,” *IEEE Transactions on Circuits and Systems for Video Technology*, vol. 28, no. 10, pp. 2513–2523, 2017.
- [28] R. Wang, X.-J. Wu, T. Xu, C. Hu, and J. Kittler, “Deep metric learning on the spd manifold for image set classification,” *IEEE transactions on circuits and systems for video technology*, vol. 34, no. 2, pp. 663–680, 2022.
- [29] I. L. Dryden, X. Pennec, and J.-M. Peyrat, “Power euclidean metrics for covariance matrices with application to diffusion tensor imaging,” *arXiv preprint arXiv:1009.3045*, 2010.
- [30] P. Li, J. Xie, Q. Wang, and Z. Gao, “Towards faster training of global covariance pooling networks by iterative matrix square root normalization,” in *Proceedings of the IEEE conference on computer vision and pattern recognition*, pp. 947–955, 2018.
- [31] M. Oquab, T. Dariseti, T. Moutakanni, H. Vo, M. Szafraniec, V. Khalidov, P. Fernandez, D. Haziza, F. Massa, A. El-Nouby, *et al.*, “Dinov2: Learning robust visual features without supervision,” *arXiv preprint arXiv:2304.07193*, 2023.
- [32] R. Sahdev and J. K. Tsotsos, “Indoor place recognition system for localization of mobile robots,” in *2016 13th Conference on computer and robot vision (CRV)*, pp. 53–60, IEEE, 2016.
- [33] A. Torii, R. Arandjelovic, J. Sivic, M. Okutomi, and T. Pajdla, “24/7 place recognition by view synthesis,” in *Proceedings of the IEEE conference on computer vision and pattern recognition*, pp. 1808–1817, 2015.
- [34] X. Sun, Y. Xie, P. Luo, and L. Wang, “A dataset for benchmarking image-based localization,” in *Proceedings of the IEEE Conference on Computer Vision and Pattern Recognition*, pp. 7436–7444, 2017.

- [35] A. Torii, J. Sivic, T. Pajdla, and M. Okutomi, “Visual place recognition with repetitive structures,” in *Proceedings of the IEEE conference on computer vision and pattern recognition*, pp. 883–890, 2013.
- [36] A. Glover, “Gardens point day and night, left and right,” *Zenodo DOI*, vol. 10, p. 3, 2014.
- [37] N. Sünderhauf, S. Shirazi, F. Dayoub, B. Upcroft, and M. Milford, “On the performance of convnet features for place recognition,” in *2015 IEEE/RSJ international conference on intelligent robots and systems (IROS)*, pp. 4297–4304, IEEE, 2015.
- [38] W. Maddern, G. Pascoe, C. Linegar, and P. Newman, “1 year, 1000 km: The oxford robotcar dataset,” *The International Journal of Robotics Research*, vol. 36, no. 1, pp. 3–15, 2017.
- [39] M. Warren, D. McKinnon, H. He, and B. Upcroft, “Unaided stereo vision based pose estimation,” in *Proceedings of the 2010 Australasian Conference on Robotics and Automation*, pp. 1–8, Australian Robotics & Automation Association, 2010.

APPENDIX CONTENTS

A Notations and abbreviations	11
B Proof of Viewpoint Robustness	11
C Proof of Illumination Robustness	12
D Analysis of Second-Order Discriminability	12
E Proof of Isometric Vectorization	13
F Qualitative Retrieval Visualization	13

APPENDIX A
NOTATIONS AND ABBREVIATIONS

TABLE V: Summary of Mathematical Notations.

Notation	Explanation
<i>Spaces and Sets</i>	
\mathcal{S}_{++}^d	The Riemannian manifold of $d \times d$ SPD matrices
$\text{Sym}(d)$	The vector space of $d \times d$ symmetric matrices
$O(d)$	The Orthogonal Group of $d \times d$ matrices ($\mathbf{Q}^\top \mathbf{Q} = \mathbf{I}$)
<i>Scalars and Hyperparameters</i>	
D_{in}	Native feature dimension of the backbone
N	Number of local patches extracted from an image
d	Dimension of the projected geometric subspace
D	Dimension of the final global descriptor
τ	Structural saliency threshold for ReCov denoising
ϵ	Regularization constant for numerical stability
K	Number of iterations for the Newton-Schulz algorithm
α	Power parameter for PEM
s	Scalar factor representing global illumination intensity
<i>Vectors and Matrices</i>	
\mathbf{I}_d	The $d \times d$ identity matrix
\mathbf{x}_i	The i -th local feature vector (column)
$\bar{\mathbf{x}}$	The mean vector of local features
\mathbf{X}_{raw}	The raw feature matrix from backbone
\mathbf{P}	The random orthogonal projection matrix
\mathbf{C}_{raw}	The sample covariance matrix computed from projected features
\mathbf{C}_{rec}	The rectified covariance matrix after sparse structural denoising
\mathbf{C}	The regularized SPD descriptor, $\mathbf{C} \in \mathcal{S}_{++}^d$
\mathbf{A}_0	The pre-normalized matrix for Newton-Schulz initialization
$\mathbf{Y}_k, \mathbf{Z}_k$	Iterative variables approximating matrix square root and its inverse
\mathbf{M}	The mapped descriptor on the linearized space
\mathbf{v}	The final isometric vectorized global descriptor
\mathbf{Q}	Orthogonal matrix representing viewpoint rotation
<i>Operators and Functions</i>	
$\ \cdot\ _F$	The Frobenius norm of a matrix
$\ \cdot\ _2$	The Euclidean (L_2) norm of a vector
$\text{tr}(\cdot)$	The trace operator
$\langle \cdot, \cdot \rangle_F$	The Frobenius inner product, $\langle \mathbf{A}, \mathbf{B} \rangle_F = \text{tr}(\mathbf{A}^\top \mathbf{B})$
$\Psi_{\text{PEM}}(\cdot)$	The Power Euclidean Metric mapping operator
$\text{vec}(\cdot)$	The isometric vectorization operator (with $\sqrt{2}$ weighting)
$\Phi(\cdot)$	The composite function of the entire descriptor generation pipeline

TABLE VI: Summary of Abbreviations.

Abbreviation	Explanation
VPR	Visual Place Recognition
SPD	Symmetric Positive Definite
6-DoF	Six Degrees of Freedom
RIA	Riemannian Invariant Aggregation
ReCov	Rectified Covariance
PEM	Power Euclidean Metric
LEM	Log-Euclidean Metric
EIG	Eigenvalue Decomposition
GeM	Generalized Mean pooling
VLAD	Vector of Locally Aggregated Descriptors

APPENDIX B
PROOF OF VIEWPOINT ROBUSTNESS

Assumption B.1. Let $\mathcal{X} = \{\mathbf{x}_i\}_{i=1}^N \subset \mathbb{R}^d$ be the set of local feature vectors. A change in viewpoint is modeled as an orthogonal transformation applied to the feature space: $\mathbf{x} \mapsto \mathbf{Q}\mathbf{x}$, where $\mathbf{Q} \in O(d)$ is an orthogonal matrix satisfying $\mathbf{Q}^\top \mathbf{Q} = \mathbf{I}$. This induces a congruence transformation on the covariance matrix: $\mathbf{C} \mapsto \mathbf{Q}\mathbf{C}\mathbf{Q}^\top$.

Theorem B.2. For any $\mathbf{C}_1, \mathbf{C}_2 \in \mathcal{S}_{++}^d$ and any orthogonal matrix $\mathbf{Q} \in O(d)$, the PEM distance with $\alpha = 0.5$ is invariant:

$$d_{\text{PEM}}(\mathbf{Q}\mathbf{C}_1\mathbf{Q}^\top, \mathbf{Q}\mathbf{C}_2\mathbf{Q}^\top) = d_{\text{PEM}}(\mathbf{C}_1, \mathbf{C}_2). \quad (13)$$

Proof. Recall that $d_{\text{PEM}}(\mathbf{A}, \mathbf{B}) = \frac{1}{\alpha} \|\mathbf{A}^\alpha - \mathbf{B}^\alpha\|_F$. With $\alpha = 0.5$, we utilize the property that matrix square root functions are equivariant under orthogonal conjugation. Since \mathbf{Q} is orthogonal:

$$(\mathbf{Q}\mathbf{C}\mathbf{Q}^\top)^{1/2} = \mathbf{Q}\mathbf{C}^{1/2}\mathbf{Q}^\top. \quad (14)$$

Substituting the transformed matrices into the distance metric:

$$d_{\text{PEM}}^2(\mathbf{C}'_1, \mathbf{C}'_2) = 4\|\mathbf{Q}\mathbf{C}_1^{1/2}\mathbf{Q}^\top - \mathbf{Q}\mathbf{C}_2^{1/2}\mathbf{Q}^\top\|_F^2 \quad (15)$$

$$= 4\|\mathbf{Q}(\mathbf{C}_1^{1/2} - \mathbf{C}_2^{1/2})\mathbf{Q}^\top\|_F^2. \quad (16)$$

Applying the unitary invariance property of the Frobenius norm ($\|\mathbf{U}\mathbf{A}\mathbf{V}\|_F = \|\mathbf{A}\|_F$ for orthogonal \mathbf{U}, \mathbf{V}), the rotation matrices \mathbf{Q} and \mathbf{Q}^\top are eliminated:

$$4\|\mathbf{Q}(\mathbf{C}_1^{1/2} - \mathbf{C}_2^{1/2})\mathbf{Q}^\top\|_F^2 = 4\|\mathbf{C}_1^{1/2} - \mathbf{C}_2^{1/2}\|_F^2 = d_{\text{PEM}}^2(\mathbf{C}_1, \mathbf{C}_2). \quad (17)$$

Thus, the distance remains invariant. \square

Remark B.3. This theorem confirms that our PEM mapping introduces the necessary non-linearity ($\mathbf{C}^{1/2}$) to flatten the manifold curvature without breaking the crucial rotational invariance. This ensures that the relative ranking between query and database images remains stable under viewpoint shifts, even when using Euclidean search engines on the mapped descriptors.

APPENDIX C PROOF OF ILLUMINATION ROBUSTNESS

Assumption C.1. Global illumination changes are modeled as a scalar multiplication of the feature vectors, leading to a quadratic scaling of the covariance matrix: $\mathbf{C} \mapsto s^2\mathbf{C}$ for some $s > 0$.

Theorem C.2. Let $\Phi(\mathbf{C})$ denote the complete descriptor generation pipeline (PEM mapping \rightarrow isometric vectorization $\rightarrow L_2$ normalization). Then for any $s > 0$:

$$\Phi(s^2\mathbf{C}) = \Phi(\mathbf{C}). \quad (18)$$

Proof. We trace the transformation of the matrix $\mathbf{C}' = s^2\mathbf{C}$ through the pipeline:

1) **PEM Mapping:** Since the matrix square root is positively homogeneous, $(\mathbf{C}')^{1/2} = (s^2\mathbf{C})^{1/2} = s\mathbf{C}^{1/2}$.

2) **Vectorization:** The vectorization operator is linear. Let $\mathbf{v} = \text{vec}(\mathbf{C}^{1/2})$. Then, $\mathbf{v}' = \text{vec}(s\mathbf{C}^{1/2}) = s \cdot \mathbf{v}$.

3) **Normalization:** The final L_2 normalization cancels the scalar s :

$$\Phi(\mathbf{C}') = \frac{\mathbf{v}'}{\|\mathbf{v}'\|_2} = \frac{s\mathbf{v}}{\|s\mathbf{v}\|_2} = \frac{s\mathbf{v}}{s\|\mathbf{v}\|_2} = \frac{\mathbf{v}}{\|\mathbf{v}\|_2} = \Phi(\mathbf{C}). \quad (19)$$

This confirms scale invariance. \square

Remark C.3. This result highlights a practical advantage of PEM over the Log-Euclidean Metric (LEM). For LEM, the mapping is $\log(s^2\mathbf{C}) = \log(\mathbf{C}) + 2\ln(s)\mathbf{I}$. This additive term $2\ln(s)\mathbf{I}$ cannot be removed by simple L_2 normalization, making LEM inherently sensitive to illumination intensity unless explicitly centered. PEM handles this naturally via homogeneity.

APPENDIX D ANALYSIS OF SECOND-ORDER DISCRIMINABILITY

Theorem D.1. There exist distinct scene distributions P_A and P_B such that their first-order means are identical ($\mu_A = \mu_B$), yet their geodesic distance on the SPD manifold is strictly positive.

Proof. Consider two scenes with centered features ($\mu_A = \mu_B = \mathbf{0}$) but distinct principal directions (e.g., vertical vs. horizontal textures). Let their covariance matrices be diagonal:

$$\mathbf{C}_A = \text{diag}(\sigma_{\text{high}}, \sigma_{\text{low}}), \quad \mathbf{C}_B = \text{diag}(\sigma_{\text{low}}, \sigma_{\text{high}}), \quad (20)$$

where $\sigma_{\text{high}} \neq \sigma_{\text{low}}$.

The Euclidean distance between their means is $\|\mu_A - \mu_B\|_2 = 0$, implying they are indistinguishable. However, the PEM distance between their covariances is:

$$d_{\text{PEM}}(\mathbf{C}_A, \mathbf{C}_B) = 2\|\mathbf{C}_A^{1/2} - \mathbf{C}_B^{1/2}\|_F \quad (21)$$

$$= 2\sqrt{(\sqrt{\sigma_h} - \sqrt{\sigma_l})^2 + (\sqrt{\sigma_l} - \sqrt{\sigma_h})^2} \quad (22)$$

$$= 2\sqrt{2}|\sqrt{\sigma_h} - \sqrt{\sigma_l}| > 0. \quad (23)$$

Since the distance is non-zero, the second-order metric successfully discriminates the two scenes. \square

Remark D.2. This example theoretically justifies the necessity of modeling scenes on the SPD manifold. By capturing the “ellipsoidal” shape of feature distributions rather than just their “centroids,” our method resolves perceptual aliasing in complex environments where mean-pooling methods fail.

APPENDIX E PROOF OF ISOMETRIC VECTORIZATION

Theorem E.1. *The vectorization operator $\psi(M)$ defined with $\sqrt{2}$ scaling for off-diagonal entries is a linear isometry between $\text{Sym}(d)$ and $\mathbb{R}^{d(d+1)/2}$ with respect to the Frobenius inner product.*

Proof. The Frobenius inner product of symmetric \mathbf{A}, \mathbf{B} is $\langle \mathbf{A}, \mathbf{B} \rangle_F = \text{tr}(\mathbf{AB}) = \sum_{i,j} A_{ij}B_{ij}$. Exploiting symmetry:

$$\langle \mathbf{A}, \mathbf{B} \rangle_F = \sum_i A_{ii}B_{ii} + 2 \sum_{i < j} A_{ij}B_{ij}. \quad (24)$$

The Euclidean inner product of $\mathbf{v}_a = \psi(\mathbf{A})$ and $\mathbf{v}_b = \psi(\mathbf{B})$ is:

$$\langle \mathbf{v}_a, \mathbf{v}_b \rangle = \sum_i (A_{ii}B_{ii}) + \sum_{i < j} (\sqrt{2}A_{ij})(\sqrt{2}B_{ij}) \quad (25)$$

$$= \sum_i A_{ii}B_{ii} + 2 \sum_{i < j} A_{ij}B_{ij} = \langle \mathbf{A}, \mathbf{B} \rangle_F. \quad (26)$$

This isometry ensures Hilbert space isomorphism, preserving the manifold’s inner product structure in the retrieval space. \square

APPENDIX F QUALITATIVE RETRIEVAL VISUALIZATION

To provide an intuitive understanding of our method’s robustness, we present qualitative retrieval results under four representative challenging conditions in Visual Place Recognition: seasonal variation, occlusion, illumination change, and perspective change.

As illustrated in Figure 5, our proposed framework exhibits robust retrieval performance across diverse challenging scenarios:

- **Seasonal Variation:** Despite drastic appearance changes caused by foliage differences between seasons, our method successfully identifies the correct location by leveraging the intrinsic geometric structure encoded in the second-order statistics.
- **Occlusion:** When parts of the scene are occluded by objects, the covariance-based representation maintains discriminative power by capturing the global structural correlations rather than relying on specific local features.
- **Illumination Change:** The theoretical scale invariance of our PEM-based pipeline (as proven in Appendix C) translates to practical robustness against day-night transitions and varying lighting conditions.
- **Perspective Change:** Viewpoint variations induce geometric transformations in the feature space. As demonstrated in Appendix B, our method’s invariance to orthogonal transformations ensures stable retrieval under camera pose changes.

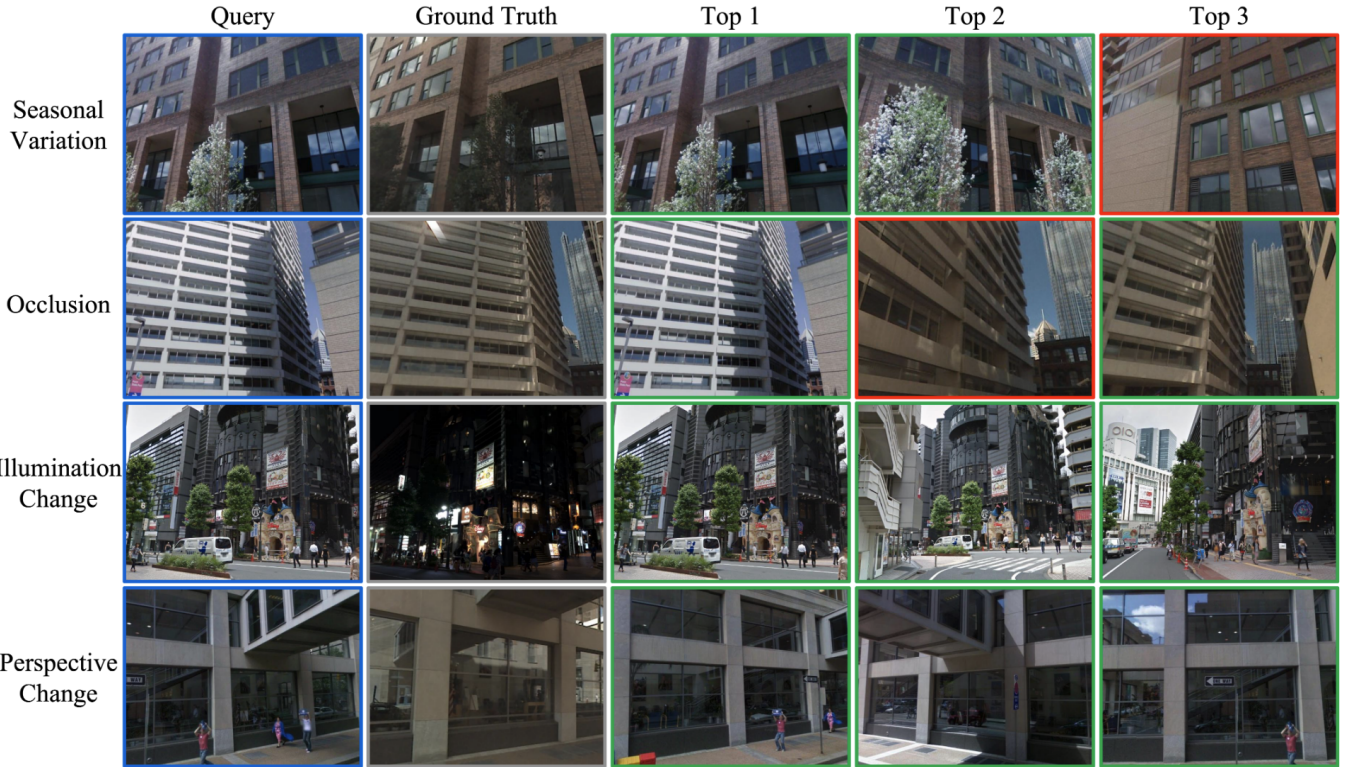


Fig. 5: Qualitative retrieval results under challenging conditions. Each row represents a different challenge scenario: (1) Seasonal Variation, (2) Occlusion, (3) Illumination Change, and (4) Perspective Change. For each scenario, we show the query image (blue border), the ground truth match, and the top-3 retrieved results. Green borders indicate correct matches, while red borders denote incorrect retrievals. Our method demonstrates strong robustness across diverse environmental perturbations, successfully retrieving correct matches even under significant appearance variations.